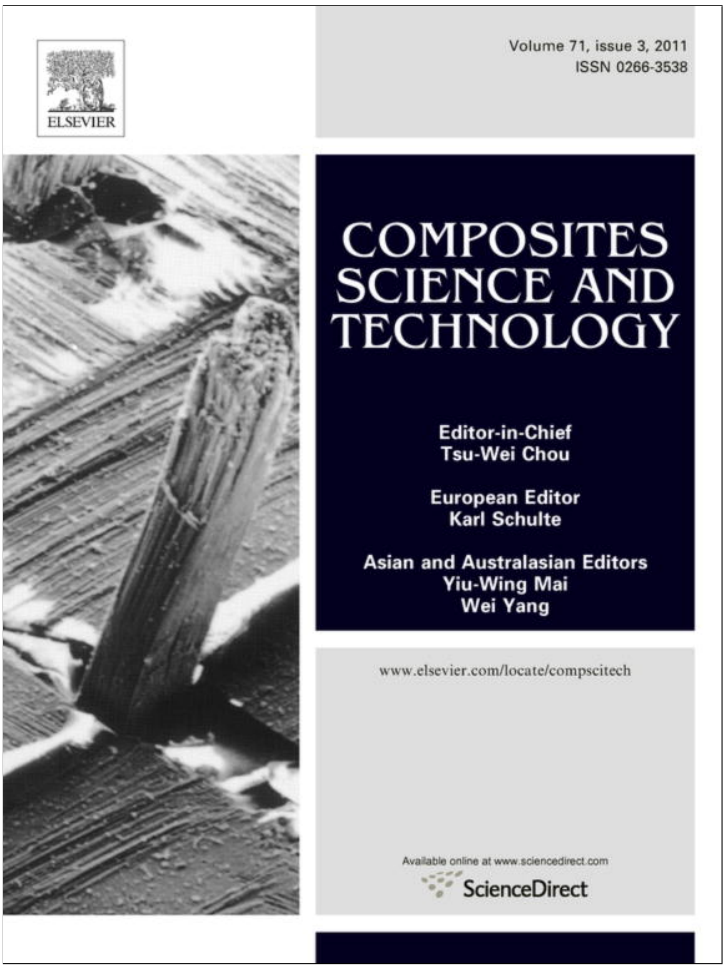

Composites Science and Technology 71 (2011) 333–342

Contents lists available at ScienceDirect

Composites Science and Technology

journal homepage: www.elsevier.com/locate/compscitech

Micromechanics of diffusion-induced damage evolution in reinforced polymers

A.S. Abhilash [a], Shailendra P. Joshi [a,*], Abhijit Mukherjee [b], Leon Mishnaevsky Jr. [c]

[a] Department of Mechanical Engineering, 9 Engineering Drive 1, National University of Singapore, Singapore 117576, Singapore
[b] Thapar University, Patiala 147 001, India
[c] Risø National Laboratory for Sustainable Energy, Materials Research Division, Technical University of Denmark, DK-4000 Roskilde, Denmark

ARTICLE INFO

Article history:
Received 6 March 2010
Received in revised form 14 October 2010
Accepted 27 November 2010
Available online 2 December 2010

Keywords:
A. Polymer–matrix composites
B. Environmental degradation
B. Debonding
C. Computational mechanics
Random microstructures

ABSTRACT

In this work we numerically investigate the nucleation and evolution of micromechanical damage in reinforced glassy polymers under transient hygro-mechanical loading. In particular, we demonstrate the role that fiber distribution plays in the evolution of overall damage due to fiber–matrix interfacial debonding under moisture ingress. The heterogeneity of fiber distribution (clustering) is characterized by the coefficient of variation C_v of the center-to-center distances between interacting fibers, determined by identifying a cut-off radius around a typical fiber. The initial moisture diffusion-induced damage provides synergistic conditions for the rapid evolution of debonding under subsequent mechanical loading. The results indicate that microstructural heterogeneity strongly affects the moisture diffusion characteristics that in turn hurt the overall load carrying capacity of a composite due to aggravated damage. The strong dependence of the moisture-induced damage evolution on the fiber arrangement suggests that one should not resort to using simplistic unit cell models that assume regular fiber arrangements in such cases.

1. Introduction

Polymers, natural or synthetic, are often reinforced with stiffer inclusions in the form of fibers or particles to create heterogeneous composites that are attractive for applications where mechanical strength and stability are of primary interest. The choice of the polymer (matrix) and inclusion (reinforcement) is dictated by the requirements of the end application. Many large-scale structural applications such as automotive, aerospace, turbine blades, etc. typically employ epoxy-based polymeric matrices reinforced with high strength synthetic fibers such as glass or carbon. Often, the differences in the physical, mechanical and chemical properties of these two constituents create a large property mismatch in the interfacial regions of the composite. Under external stimuli, high stresses tend to concentrate around these interfacial regions and this may potentially lead to overall composite degradation through a variety of microstructural instabilities including interface debonding, fiber breaking, void nucleation and shear localization in the matrix that are precursors to the macro-structural failure. It has long been recognized that while polymer composites possess exceptional potential in designing light and strong applications, their use may be limited by the fact that their response to environmental conditions during their functional life is not well understood. This is especially critical when one recognizes that they are deployed in protean service environments and are expected to perform over long periods of time. Residual stresses occur in a composite subjected to varying temperature or moisture conditions, due to the difference in the thermal or moisture expansion coefficients between the fiber and the matrix. In particular, moisture ingress may assist the degradation of composites, possibly further amplified by temperature, that may be detrimental, for example, wind energy or marine structures that experience a range of changes in temperature and moisture (salinity may have additional effects) in addition to the regular mechanical loads [1,2]. Composites used for dental restoration purposes may experience aqueous service environments that range between strongly acidic to strongly alkaline [3]. Further, the moisture diffusivity itself may be a function of the applied stress, which in turn may affect the stress distribution in the composite [4–6]. The absorbed moisture may lead to matrix cracking [7–11] or plasticize the matrix thereby reducing effective stiffness and strength of polymers [7] and their composites [1,2,12]. An efficient design of a composite for specific functions relies heavily on the ability to predict the possible mechanisms of failure at multiple length and time-scales when subjected to such synergistic environments [13,14]. These effects may be further complicated by the fact the most composite micro-architectures exhibit random inclusion topologies. The aforementioned scenarios pose challenges for engineers and necessitate a better understanding of the mechanical behavior of such heterogeneous micro-architectures in hostile environments as a function of microstructural details.

* Corresponding author. Tel.: +65 6516 4496; fax: +65 6779 1459.
E-mail address: Shailendra@nus.edu.sg (S.P. Joshi).

0266-3538/$ - see front matter © 2010 Elsevier Ltd. All rights reserved.
doi:10.1016/j.compscitech.2010.11.027

In this work, we numerically investigate the response of reinforced glassy polymers under transient hygro-mechanical conditions at the microstructural length-scale. We focus on modeling the nucleation and evolution of damage at the micromechanical scale in a model glass-reinforced epoxy polymer composite subjected to moisture and mechanical loads under isothermal conditions. Of the above-mentioned possible microstructural modes of failure, we explicitly model the experimentally observed debonding at the matrix-inclusion interfaces due to moisture-induced stresses [2,15,16]. Such debonded interfaces may act as the channels causing accelerated diffusion especially if it is in the exposed surface [17]. Further, some experiments on glass fiber–epoxy matrix composites have revealed that both the strength and toughness of the fiber–matrix interfaces may degrade significantly in moist environments exacerbating the severity of damage [2,18]. Motivated by these experimental observations (see also [19]), we incorporate the possibility of the interface behavior that continuously degrades with the evolution of local moisture concentration. While the moisture diffusion and stress build-up phenomena in composites have been modeled by researchers (e.g. [20,21]), there are relatively few works that model the evolution of hygro-mechanically induced damage, in general (e.g. [6,22]) and interface failure, in particular (e.g. [23]). Some works that do model interfacial effects under hygral or thermal excursions resort to the restrictive assumption of unit cells with regularly arranged fibers (e.g. [24]), which is seldom the case in real materials [25]. In fact, the effective diffusivities may strongly be affected by the tortuosity of the microstructure, which may have direct implications on the build-up of differential stresses [21,25,26]. In this work, we relax this restriction by choosing representative volume elements (RVEs) with random arrangements alongside the regularly arranged RVEs. In précis, the objective of this work is to develop a predictive approach to characterize moisture diffusion-induced damage incurred through interfacial failure in reinforced polymers as a function of microstructural randomness and its effect on the subsequent response when loaded mechanically. In the next section, we describe the computational setup and the details of the finite element (FE) models used in the investigation.

2. Computational modeling

Fig. 1 shows a typical section of a unidirectionally reinforced lamina of thickness $2L_2 = 100$ μm [13] in the X_2-direction considered in the present work. We consider the lamina to be infinitely long in the X_1-direction, comprising repeating unit cells giving a periodic RVE in that direction (shown in the figure by the dashed box). Further, we assume that the lamina is symmetric about $X_2 = 0$ and satisfies the plane-strain condition in the X_3-direction. Within an RVE the fibers may be arranged in a regular or random manner. The top and bottom surfaces of the lamina may be subjected to mechanical and/ or moisture boundary conditions (bc's).

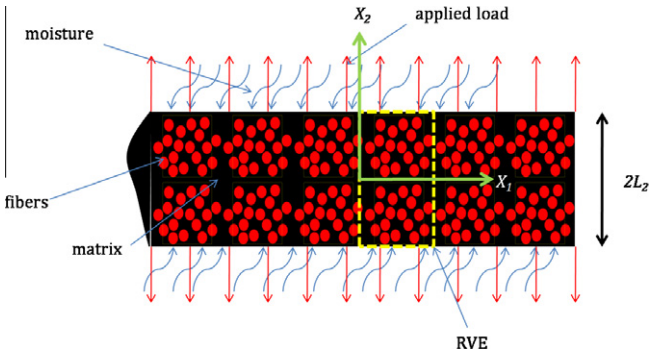

Fig. 1. A unidirectionally reinforced composite lamina subjected to mechanical and moisture boundary conditions. The lamina is periodic in the X_1-direction. A typical RVE considered in the computational modeling is shown by the dashed boundary.

2.1. RVE generation and characterization of micro-architectures

Microstructural characterizations of real composites unequivocally reveal the random topological arrangements of fibers (e.g. [27,28]). While one may use digitized versions of such real microstructures, we adopt a more computational approach in that we generate artificial microstructural arrangements mimicking real composites [29]. Such a strategy enables comparing a wide range of microstructures with different fiber volume fractions f, arrangements and fiber diameters, d. As an example, Fig. 2a–f shows six of the nearly 50[1] different RVEs considered in this work that are generated using an in-house code for two-dimensional (2D) heterogeneous composite micro-architectures with desired fiber arrangements (regular/random and uniform/clustered), for a given fiber diameter d and f. Specifically, these RVEs are constructed for fixed $f = 0.47$ for all the random arrangements and equal to 0.50 for the two regular arrangements to investigate the effects of fiber distribution. These volume fractions are represented by 15 (16 in the case of the regular arrangements) 10 μm diameter fibers [30], which also sets up the size of the RVE. The RVEs in Fig. 2a–c are three different random (R1, R2, R3) arrangements. Note that amongst these three the R2 arrangement has all the fibers completely inside the RVE, which means that there exists a thin *matrix-rich* layer at the edges of the RVE [25]. Fig. 2d shows a random arrangement but with a clustering (RC) of fibers leaving what appears to be a big region in the microstructure that is matrix-rich. Fig. 2e shows the regular square (SR) arrangement, used as benchmark. Finally, Fig. 2f shows the square clustered (SC) arrangement where a set of four fibers are placed close together and this arrangement is repeated within the RVE. This description of the RVEs with random fiber arrangements is qualitative. In literature, different approaches have been formulated to characterize the topological disorder in composite microstructures. Pyrz and Bochenek [31] defined topological entropy based on the Dirichlet tessellation method and correlated it with the microstructural stress field in fiber composites. Chen and Papathanasiou [28] used a second-order intensity function based on a cut-off radius and the number of fibers within that zone to characterize different fiber arrangements. Based on an exclusion probability defined by Torquato [32] few others [33,34] used the nearest neighbor distance. In this work, we quantify the heterogeneity of fiber distribution (i.e. clustering) in different RVEs using the center-to-center (c–c) distance between the neighboring fibers. The neighbors of a fiber are defined such that the lines joining the centers of two fibers do not trespass other fibers. Then, the coefficient of variation $C_v(=\Sigma/\mu$, Σ = standard deviation and μ = mean) of the c–c distance can be used as a metric to quantify clustering. Fig. 3 shows an example for the random arrangement with $d = 10$ μm and $f = 0.47$. Green circles are the fibers, the magenta outline represents the periodicity of the RVE, and the blue and red lines connect the centers of fibers such that none of the lines pass through an intermediate fiber. Note that the red lines connect fibers that are significantly apart from each other even though they may not necessarily *communicate* with each other through their stress fields, yet they can be connected topologically as far as the definition of c–c connectivity is concerned. From a topological perspective, this situation may not be uncommon in random microstructures; however, from the physical viewpoint it may not be relevant to include such remote influences. An important question then arises: for a given fiber, how many surrounding fibers influence its failure? In other words, is there a cut-off radius r_c that

[1] These include RVEs for different volume fractions (vf) ($f = 0.30, 0.40, 0.50, 0.60$) and diameters ($d = 9, 10, 11$ μm).

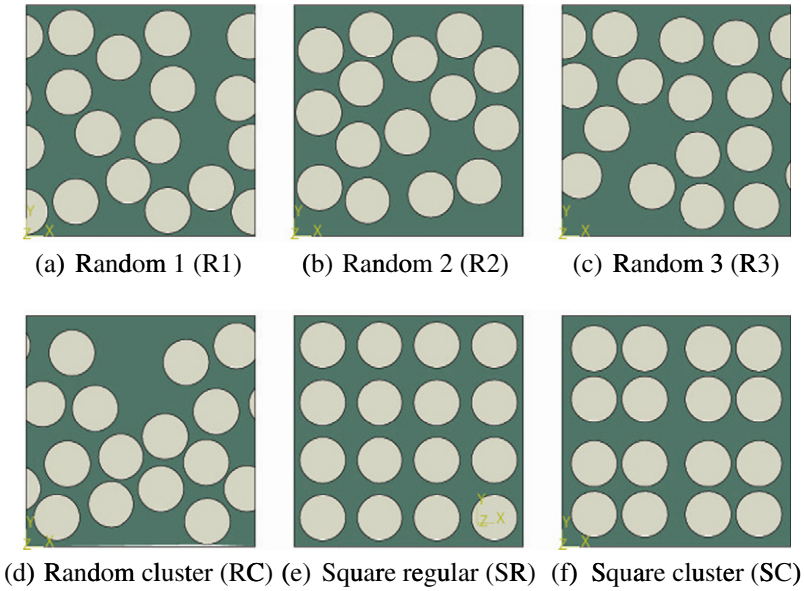

Fig. 2. RVEs with different fiber arrangements with $f = 0.50$ and $d = 10$ μm.

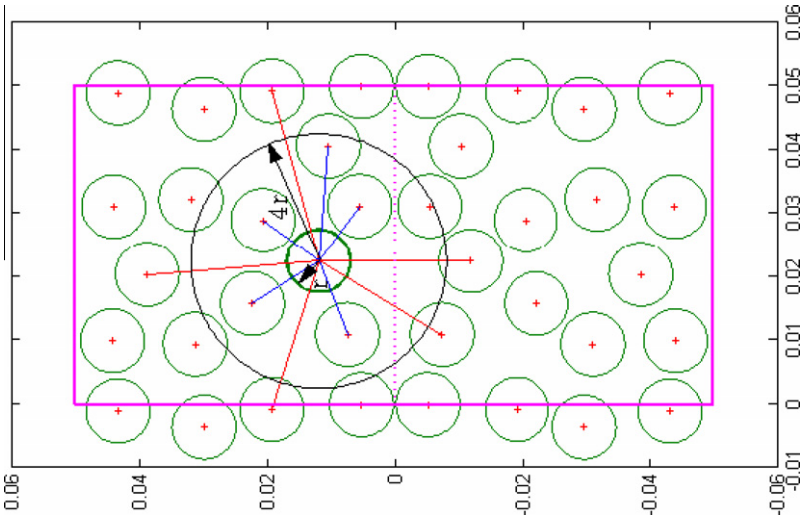

Fig. 3. Illustration showing the calculation of C_v based on cut-off radius r_c for an RVE (see Section 2.1 for details).

can be used in determining C_v? From a stress concentration argument, one may consider that fibers that are farther than ~ 1–2 diameters away from the fiber edge may not significantly influence its failure. Referring back to our example in Fig. 3, for a fiber at the center, the neighborhood of influence with $r_c = 4r$ (where $r = d/2$) and the c–c lines falling within this cut-off are shown by blue lines and are used to calculate a C_v; the red lines exceed this distance and are ignored in the calculation of C_v. As such, the C_v for a given RVE then depends on the chosen r_c. Therefore, to evaluate its influence we chose three different r_c's to calculate the relevant c–c distances, namely, $4r$, $4.5r$ and $5r$ (so that the edge-edge distance between any two interacting fibers are $\leqslant 2r$, $2.5r$ and $3r$, respectively). This also partly accounts for the next nearest neighbor interactions. In Section 3.3, we discuss the correlation between C_v's defined this way and the overall damage. We demonstrate that the degree of overall damage correlates well with the C_v across protean RVEs with different distributions, vf's and diameters.

In order to ensure proper modeling of the fiber–matrix interfaces we do not allow a fiber touching another. The topological periodicity of the fiber arrangement is ensured at the left and right edges of the RVE and is also specified in terms of the coupling between the kinematic boundary conditions (bc's) at these edges as discussed in the next section.

2.2. Finite element model

An important aspect of this work is to model the transient moisture diffusion, which is assumed to obey Fick's law. The Fick's law is analogous to the Fourier's heat conduction law [20], which is available in ABAQUS/Standard® FE program [35] as a coupled temperature–displacement analysis procedure. We exploit this analogy to model the transient, coupled moisture–displacement problem. The moisture diffusivity (D_m) is specified in terms of the equivalent thermal diffusivity (D_t) in ABAQUS.[2] The temperature evolution in the RVE then resembles the moisture diffusion. Likewise, the moisture bc is specified in terms of an equivalent tem-

[2] In ABAQUS, $D_t = \frac{k}{\rho c_p}$, where k is the thermal conductivity, ρ the mass density and c_p the specific heat. However, it is the ratio that is important rather than the values of the individual parameters.

Table 1
Material properties for the fibers and matrix used in the simulations.

	Elastic modulus, E (GPa)	Poisson's ratio, ν	Diffusion coefficient, D (mm^2/s)	Moisture expansion coefficient, β (/%H_2O)
Fiber	75	0.28	0	0
Matrix	4	0.38	54×10^{-8}	3.24×10^{-4}

perature. Note that the thermal–moisture *direct* analogy [36] adopted here is valid only as long as only one of the phases is capable of moisture diffusion,[3] which is true in the present work. The micro-architectures generated by the code are imported into ABAQUS and meshed using the plane strain, linear quadrilateral finite elements with displacement and *moisture* degrees of freedom (CPE4T). In our calculations, a typical RVE comprises ~30,000 finite elements after conducting mesh convergence with different mesh densities for a few cases. The periodic mechanical bc's applied to the left and right edges may be expressed in terms of the relative displacement vector $\vec{U}_1 = u_1(0, X_2) - u_1(L_1, X_2)$ between the opposite edges of an RVE, $X_1 = 0$ and $X_1 = L_1$ [37], where u_1 is the displacement in the X_1-direction and L_1 sets the wavelength of the periodicity. The vector $\vec{U}_1$ is computed from the condition that $\int_0^{L_2} \boldsymbol{t}\, dX_2 = 0$ on $X_1 = 0$ and $X_1 = L_1$, where $\boldsymbol{t}$ is the traction vector. On the top and bottom edges both displacement and moisture bc's may be present. The average strain due to an applied uniform displacement $u_2(X_1, L_2)$ in the X_2-direction is, $\bar{\varepsilon}_{22} = u_2/L_2$ and the corresponding average stress is $\bar{\sigma}_{22} = \frac{1}{L_1}\int_0^{L_1} \sigma_{22}(X_1, L_2)dX_1$.

2.3. Constitutive laws

In the present case, a linear, hygro-elastic constitutive law,[4] $\boldsymbol{\sigma} = \mathbf{E} : [\boldsymbol{\varepsilon} - \beta(c - c_0)\mathbf{I}]$ is adopted for the matrix phase, where $\boldsymbol{\sigma}$ is the stress tensor, $\mathbf{E}$ is the fourth-order elasticity tensor, $\boldsymbol{\varepsilon}$ is the total strain tensor. β is the isotropic coefficient of moisture expansion defined for the percentage by weight of the moisture absorbed by the matrix, $c\left(= \int_0^t \dot{C}(t')dt'\right)$ is the moisture concentration at time t, c_0 is the reference moisture concentration and $\mathbf{I}$ is the identity tensor. The moisture evolution follows Fick's law $\dot{c} = D_m \nabla^2 c$, where D_m is the matrix moisture diffusivity and ∇^2 is the Laplacian. Like the matrix, the fibers are also assumed to be linearly elastic and isotropic, but impermeable. Table 1 lists the material properties that are representative of an epoxy resin and E-glass fiber [21,30], where the elastic properties of the epoxy correspond to the glassy regime. While it has been observed that moisture may degrade the elastic properties of some epoxies [7,11,38], the effect is much more severe and irreversible in the transition and rubbery regimes (attributed to chain scission processes) than in the glassy regime where it can at times be largely reversible [39,40]. While recent atomistic simulations attempt to address the deterioration of the glassy elastic modulus the underlying mechanisms are not fully unraveled [38,41]. In this work focusing on the glassy regime, we do not consider the elastic degradation of polymer. We also ignore plasticization effects (i.e. lowering of glass transition temperature) given that the simulation time-scales are much shorter than the typical viscoelastic time-scales for epoxies.

2.4. Interface cohesive behavior

Fiber–matrix interfaces are considered as a cohesive surface and its constitutive description is provided by a traction–separation law [35]. A linear, elastic traction–separation law $\{\vec{\mathbf{t}}\} = [\mathbf{K}]\{\vec{\boldsymbol{\delta}}\}$ is adopted, where $\{\vec{\mathbf{t}}\}$ is the nominal interface traction vector with component t_n in the normal direction and t_s in the shear direction, $\{\vec{\boldsymbol{\delta}}\}$ is the vector of displacement jumps across the interface having components δ_n and δ_s and $[\mathbf{K}]$ is the interfacial stiffness matrix. The interface debonding initiates when the magnitude of the nominal stress in the normal (n) or tangential (s) directions reach their critical values, N or S, respectively (Fig. 4) given by the softening condition $\left(\max\left\{\frac{\langle t_n\rangle}{N}, \frac{t_s}{S}\right\} = 1\right)$. The subsequent softening behavior at an interface node is governed by the damage variable $\phi = \frac{\bar{\delta}\left(\bar{\delta}^{max} - \bar{\delta}^0\right)}{\bar{\delta}^{max}\left(\bar{\delta}^f - \bar{\delta}^0\right)}$, where $\bar{\delta} = \sqrt{\langle\delta_n\rangle^2 + \delta_s^2}$. The value of $\bar{\delta}$ when the failure begins is given by $\bar{\delta}^0$ and the interface fails completely when reaches $\bar{\delta}$ reaches the value $\bar{\delta}^f$. $\bar{\delta}^{\max}$ is the maximum value of $\bar{\delta}$ at any given instant of time. Note that at a given interface node, $0 \leqslant \phi \leqslant 1$, where the lower limit denotes that the interface is intact at that node and the upper limit denotes complete separation at that node. We assume that both the normal and tangential displacement jumps contribute to the failure which is modeled via a mixed mode based failure criterion, $\left(G_n/G_n^c\right) + \left(G_t/G_t^c\right) = 1$, where G_n^c and G_t^c are the mode-I and mode-II energy release rates. As both the fracture modes contribute toward failure, an interface may fail before the failure energy reaches the critical value in any of the directions.

As noted earlier, some experiments indicate that the interface strength and toughness may be affected by moisture [2,19]. We account for this possibility by allowing the normal and shear tractions to degrade with moisture (Fig. 4). Note that in both the *moisture-resistant* (i.e. interface strength unaffected by moisture) and *moisture-affected* scenarios the interfaces may still debond, but the later will be much softer than the former. Irrespective of the nature of the interfaces we assume the final failure to occur at the same displacement $\bar{\delta}^f$; consequently, the fracture energy (i.e. the area under the traction–separation curve) is smaller for a moisture-affected interface. For calculation purposes, we assume that the critical fracture energies linearly degrade to half their original values as the local moisture concentration reaches the ambient value.

3. Results

In this section, we consider different scenarios that involve moisture and mechanical bc's. In Sections 3.1 and 3.2, we discuss all the results pertaining to the six RVEs shown in Fig. 2 that constitute a fixed fiber diameter (d = 10 μm) and nearly the same f (~0.47–0.50). Section 3.3 expands the discussion to a range of f and d. In Section 3.1, we consider the RVEs subjected only to the moisture bc. In this case, we investigate the evolution of damage due to debonding as a function of the fiber arrangements for moisture-resistant and moisture-affected interfaces. We choose the moisture bc that represents the typical weight gain at saturation in reinforced polymers exposed to moisture. For example, the saturation weight gain in glass-reinforced epoxy composites at 85% relative humidity and 85 °C is approximately 1.5% of the initial weight. These values mimic the accelerated conditions that are typically resorted to in laboratory-scale experiments [20] and we apply this moisture bc c_∞ = 1.5%. Later, in Section 3.2, we consider

[3] Alternatively, one may adopt a normalized analogy [36], which can be used under a generalized case of a bi-material system where both the phases are pervious.

[4] The operation **A**:**B** denotes a contracted product between two tensors or between a tensor and a vector.

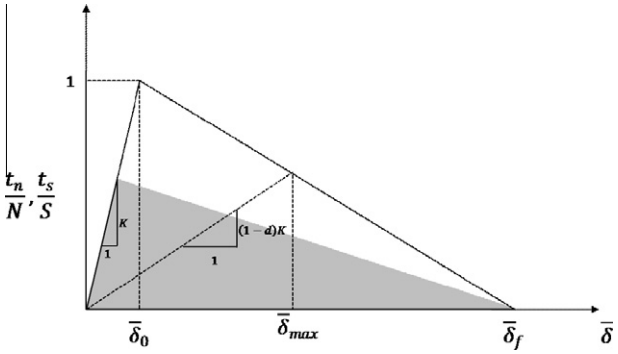

Fig. 4. The traction–separation law used for modeling fiber–matrix interface. The shaded triangle shows the degraded traction–separation rule when the moisture concentration at an interface reaches a critical value.

the cases where the moisture and mechanical bc's are applied sequentially.

3.1. Moisture induced debonding

The RVEs in Fig. 2 are subjected to moisture bc on the top edge. As moisture diffuses through the matrix, differential expansion between the matrix and fibers induce interfacial stresses that may nucleate debonding and lead to progressive damage evolution. We quantify the overall damage sustained by an RVE at time t by an aggregate damage parameter $\psi(t) = \frac{1}{n}\sum_{i=1}^{n}\phi_i \quad (0 \leqslant \psi \leqslant 1)$, where ϕ_i is given in Section 2.4 and n is the total number of nodes at all the interfaces in a RVE. Here, the physical time considered is long enough for the moisture to equilibrate throughout in RVEs.

3.1.1. Damage evolution: moisture-resistant interfaces

To begin with, we consider moisture-resistant interfaces so that the interfacial strengths ($N = S = 25$ MPa) and fracture energies ($G_n^c = G_t^c = 50\ \mathrm{J/m^2}$) are unaltered even in the presence of moisture [30,42]. Figs. 5a and b show the temporal evolution of ψ in the six RVEs and its dependence on the their topological descriptor, C_v, respectively. For fixed f the damage evolution is significantly different depending upon the micro-architecture and for the applied bc the RC-RVE (largest C_v) sustains the maximum overall damage while the SR arrangement (lowest C_v) experiences no damage at all. Note that for different f's and fiber diameter d, it is possible that even SR-RVE may exhibit damage; however, it is almost always the case that SR-RVE sustains the least overall damage. This emphasizes the strong influence of the fiber arrangement on the damage evolution under moisture ingress. For the specific cases considered in this section, the SR-RVE is the least clustered arrangement (as expected) and sustains least (no) damage, whereas the RC-RVE is the most clustered (highest C_v) and sustains most damage. Indeed, for the six RVEs shown here, the $C_v - \psi$ follows a simple linear relation (Fig. 5b). As will be shown in Section 3.3, for different f's and d's, the clustering effect quantified by C_v correlates linearly with the overall damage ψ sustained due to moisture ingress by the RVEs.

A common feature between all the arrangements except the SR arrangement is that there are matrix-rich pockets present due to some amount of fiber clustering. It is interesting to note the pattern of evolution of damage between the SC, R1 and RC arrangements. The overall damage evolution is nearly the same in the three arrangements up to about 20 min after which the rate of growth in SC falls appreciably. However, the aggregate damage in RC and R1 RVEs continue to grow almost identically much further ($t \sim 60$ min). By this time the moisture has diffused through almost half the thickness of the RVEs. If we consider the top half of all the RVEs, the R1 and RC arrangements have more matrix-rich regions compared to the other RVEs, which results in the similar response of R1 and RC arrangement. Fig. 6 compares the distribution of the third invariant $J_3 = (\frac{9}{2}[\mathbf{S}\otimes\mathbf{S}] : \mathbf{S})^{\frac{1}{3}}$ of the deviatoric stress tensor $\mathbf{S}$, for the SR, R3 and RC arrangements when the steady-state condition is reached ($\dot{c} = 0$). The J_3 invariant combines the influence of all the stress components, but also distinguishes between the tensile and compression regions (unlike the von-Mises invariant) and therefore, provides an indication of the hot-spots that are susceptible to interfacial damage. The SR-RVE deforms uniformly except at the top edge, which deforms freely to satisfy the traction bc. In comparison, the R3 and RC arrangements experience a non-uniform distribution of highly stressed regions that also sustain severe deformation than the other parts within the RVE resulting in heavy debonding. The debonding in the RC arrangement is much more severe than the other two arrangements. Further, we observe that in the RC arrangement debonding is nearly aligned with the X_1-direction unlike the SR and R3 that tend to debond along the X_2-direction.

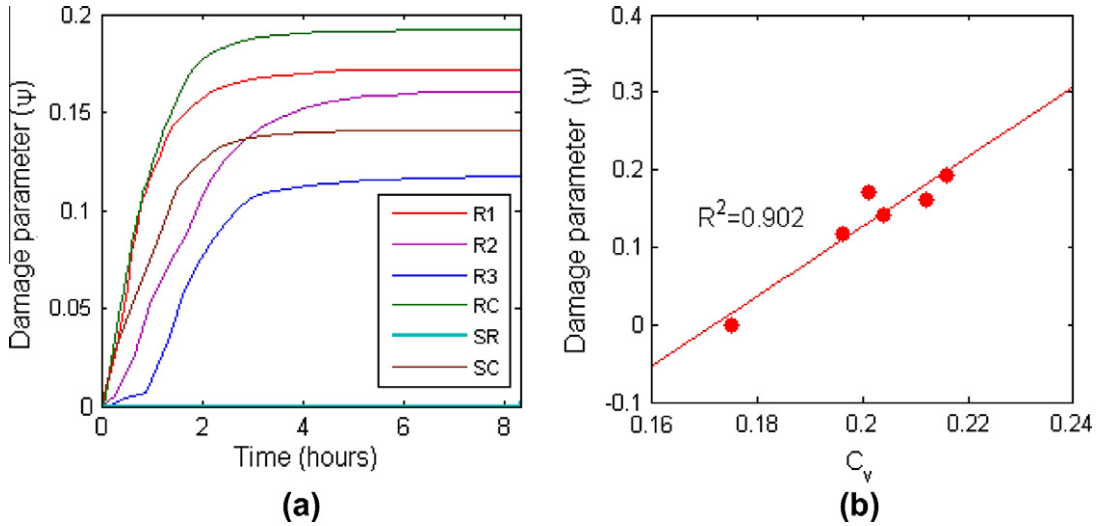

Fig. 5. (a) Evolution of the overall interface damage ψ, and (b) $\psi - C_v$ correlation between damage for $f = 0.50$ and $d = 10$ μm with (a) $r_c = 4r$, (b) $r_c = 4.5r$, and (c) $r_c = 5r$. Moisture-resistant interfaces.

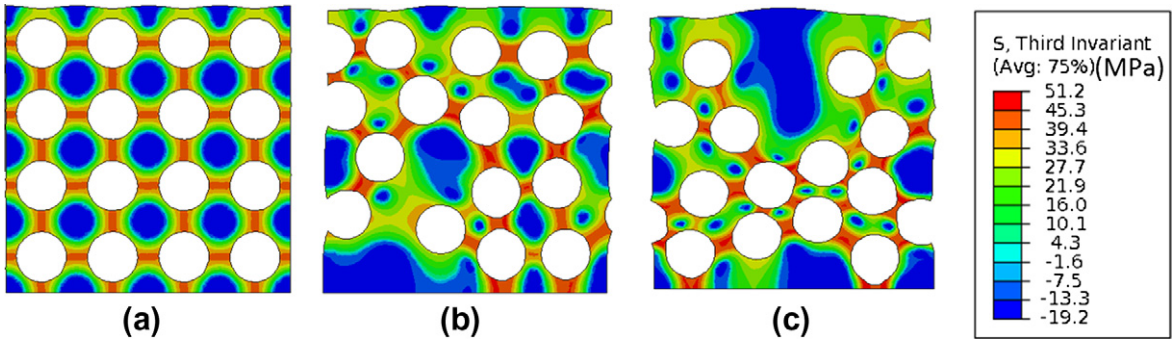

Fig. 6. Distribution of the third invariant of the deviatoric stress tensor in (a) SR, (b) R3 and (c) RC arrangements corresponding to the time at which the RVE attains equilibrium concentration in the entire domain (moisture-resistant interfaces). The deformed profiles are scaled fifty times and fibers are removed for clarity.

3.1.2. Damage evolution: Moisture-affected interfaces

To investigate the effect of degrading interfaces on the damage evolution we now allow the cohesive strength to weaken with the local moisture concentration keeping all other parameters the same as in the previous case. A key question we ask is: what is the influence of degrading interfaces on the damage evolution with reference to the trends observed in the preceding sub-section? To answer this question the initial (at $c = 0$) interfacial strengths (=25 MPa) and energies (=50 J/m^2) are now assumed to linearly degrade to 50% (shaded area in Fig. 4) as the local moisture concentration reaches its maximum value [19]. Fig. 7a shows the evolution of ψ for the six RVEs under the applied moisture bc of $c_\infty = 1.5\%$ at the top edge. As expected the overall damage in each of the RVEs is more severe than their preceding moisture-resistant counterparts, because the interfaces become progressively weaker with the evolution of the local moisture concentration. The severity of damage is emphasized from the fact the SR arrangement, which showed no damage in the preceding case, too exhibits some

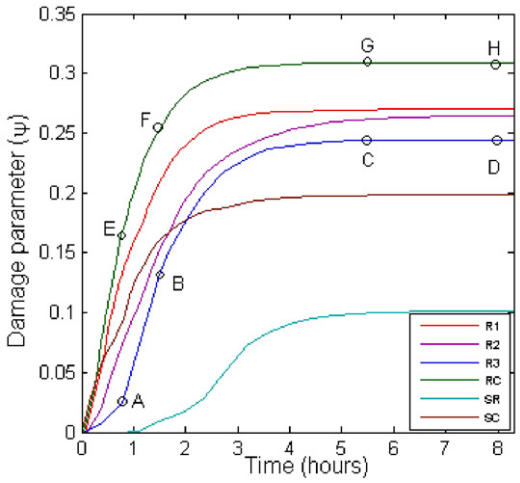

(a)

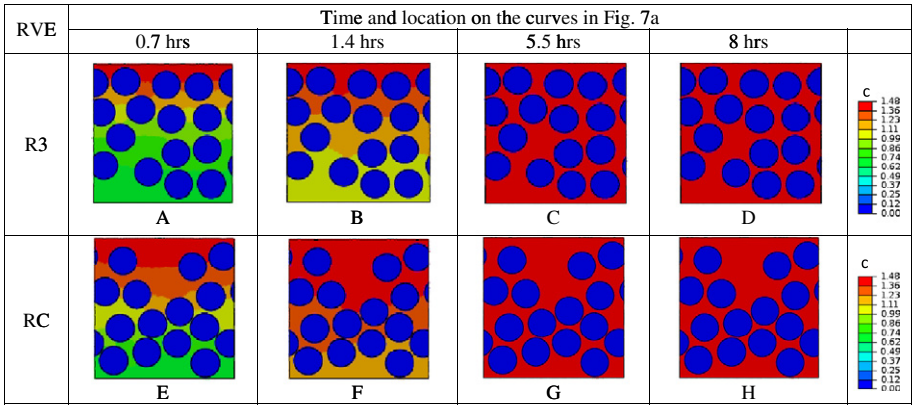

(b)

Fig. 7. Diffusion-induced evolution of interface damage ψ for moisture-affected interfaces. The open circles indicate the location of the snapshots shown in (b). (b) Snapshots of moisture diffusion profiles for the R3 and RC arrangements at $t = 0.7$, 1.4, 5.5 and 8 h. Note the higher rate of diffusion in the RC-RVE.

damage, although it is still the lowest amongst all the six RVEs. These observations suggest that it is important to rigorously characterize the effect of moisture on the interface behavior and is vital to predicting the overall composite response. The overall trends of damage evolution for other RVEs are qualitatively similar to those in Fig. 5a although there are a few differences especially at later stages. The damage evolution in the R2 and R3 arrangements is initially slow in comparison to the SC arrangement, but evolves faster beyond $t \sim 1.6$ h.

In determining the influence of a microstructure on the diffusion-induced damage one has to consider two microstructural aspects: (a) the degree of fiber clustering and (b) tortuosity [43]. In the present context, while the former is described here by C_v, the later may be described by the time it takes for moisture to fully equilibrate in an RVE. The longer the time taken the more tortuous a microstructure is and smaller is its apparent diffusivity. As an example, we compare the tortuosities vis-à-vis the overall damage sustained in the SR (lowest C_v, lowest damage), R3 (least overall damage amongst all random arrangements with $f = 0.47$, $d = 10$ μm) and RC (most severe overall damage) RVEs. Fig. 7b shows the snapshots of the moisture concentration contour for the RC and R3 arrangements at different times. In the present context of diffusion-induced damage, we define a normalized tortuosity, $\xi = t_c/t_m$, where t_c is the time required for moisture saturation in an RVE with a given f and characteristic dimension (in the diffusion direction) L_2, and t_m is the corresponding time required for moisture saturation in bare matrix with the same characteristic dimension.[5] As per this definition, although the SR-RVE is less clustered ($(C_v)_{SR} \sim 0.17$) than the RC-RVE ($(C_v)_{RC} \sim 0.25$), they exhibit similar tortuosities ($\xi_{SR} \sim 9.1$, $\xi_{RC} = 9$). However, the RC-RVE experiences significantly higher damage ($\psi_{RC} \sim 0.31$) than the SR-RVE ($\psi_{SR} \sim 0.1$) (Fig. 7a). Between the two random arrangements, the R3-RVE is less clustered ($((C_v)_{SR} \sim 0.227)$), more tortuous ($\xi_{R3} \sim 11$), but sustains lesser damage ($\psi_{R3} \sim 0.24$) than the RC-RVE. That is, unlike C_v, ξ does not show a consistent correlation with damage. In other words, this suggests the C_v and ξ do not necessarily correlate in a simple (monotonic, linear) manner like the $C_v - \psi$ relation (Section 3.3). This is because, while C_v compares different RVEs purely from the topological viewpoint, ξ involves a spatio-temporal description that depends on the resistance to moisture ingress along the direction of moisture ingress. This can be most easily illustrated by considering an RVE, say RC, and switching the plane of symmetry with the direction of moisture ingress. Although not shown here, in this scenario the C_v of the *flipped* RC-RVE is the same as its original version, but is more tortuous. In summary, clustering is a topological descriptor that can be used to describe the severity of damage vis-à-vis microstructural spatial heterogeneity, whereas tortuosity has to be determined with reference to the direction of diffusion and may not give a systematic correlation with damage, although it may have an influence on the damage.

3.2. Mechanical loading of initially damaged microstructures

While composite microstructures that have sustained initial damage such as that induced due to moisture ingress are expected to demonstrate a compromised response compared to their pristine counterparts when subsequently subjected to mechanical stimuli. A natural question that then arises is: how does this initial diffusion-induced damage incurred in the microstructures affect the performance when subjected to mechanical stimuli? Does microstructural disorder still dictate the further evolution of damage and affect its stiffness and the aggregate (stress–strain) response? If so, what degree does it affect? To answer these questions, we examine the response of the initially damaged (due to moisture) microstructures in the presence of applied mechanical load. A displacement bc (resulting in the macroscopic final strain = 3%) is applied on the top face of each of the six RVEs considered in the preceding section after the moisture has completely equilibrated and the diffusion-induced damaged has saturated. We simulate this as a two-step loading case in ABAQUS/STANDARD, where in the first step the moisture bc is applied and when moisture fully saturates, the second step corresponding to the mechanical bc is invoked. Fig. 8 shows the average stress ($\bar{\sigma}_{22}$) –strain ($\bar{\varepsilon}_{22}$) response of the six RVEs. For brevity, we show only the results for the moisture-affected interfaces as the results for the moisture-resistant interfaces are qualitatively similar. In Fig. 8 the initial stress-free strain corresponds to the first step that evolves due to the constrained moisture expansion of the RVEs. The stresses due to the constraint from the fibers are locked in the matrix and fibers as residual stresses, but do not manifest themselves in the stress–strain response as they self-equilibrate. However, these stresses play a vital role in determining the response of the RVEs in the subsequent mechanical loading step. As noted in the preceding section the interface debonding initiates due to moisture ingress. In the two-step loading, this initial diffusion-induced interfacial damage leads to an overall softer average stress–strain response in all the RVEs compared to the cases where the interfaces do not encounter moisture-induced stresses. This is clearly reflected in Table 2 that shows the initial tangent moduli (calculated at small times in the second step). The moduli of the initially damaged RVEs (in both, the moisture-resistant and moisture-affected cases) are ~10–30% lower than their corresponding pristine interface counterparts. As the loading progresses the stress–strain response becomes nonlinear due to the rapid evolution of damage.

An interesting aspect comes to the fore when one observes the modulus degradation for the SR arrangement with moisture-resistant interfaces (Table 2). Note that in case of the moisture-only bc (with $c_\infty = 1.5\%$) this arrangement does not exhibit any damage (Fig. 5a); however, post-equilibration it shows a substantial drop in the initial tangent modulus of nearly 20% upon application of a small mechanical load. This indicates that the debonding commences as soon as the SR composite is loaded mechanically. The reason for such a sudden decrease in the stiffness is explained as follows: During the moisture diffusion step the ligaments connecting a column of fibers experience tensile stress in the X_2-direction. This also induces a tensile stress at the interfacial regions near the top and bottom (the *poles*) of each fiber (Fig. 6a). In the subsequent step, when a mechanical load is applied in the same direction the normal stresses in the ligaments along the loading direction superpose with the initial residual stresses causing the interfaces to instantaneously debond as the total stress exceeds the critical value. As the SR-RVE comprises regular fiber arrangement the stress state is identical at all the poles (except those near the top edge due to boundary effects) causing simultaneous failure of all the interfaces near the poles. A similar characteristic is also observed in the R3 arrangement (Fig. 6b), which has two columns of fibers that are nearly aligned.

It is interesting to note that although the RC arrangement sustains the maximum overall damage at the end of the moisture step (c.f. Figs. 5a and 6c) it is the R3, SC and SR arrangements that show the largest drops in their tangent moduli in both the moisture-resistant and moisture-affected scenarios (Table 2). This phenomenon is ascribed again to the location of the debonding with respect to the loading axis. For the SR, SC and R3 arrangements it is the interfacial regions near the fiber poles that debond as these architectures resemble columnar fiber arrangements. In contrast, in the RC arrangement that does not show the tendency

[5] Alternatively, $\xi = \frac{\Delta x_c}{\Delta x_m}$, where Δx_c and Δx_m = distance traversed by moisture along the diffusion direction per unit time in an RVE and bare matrix, respectively.

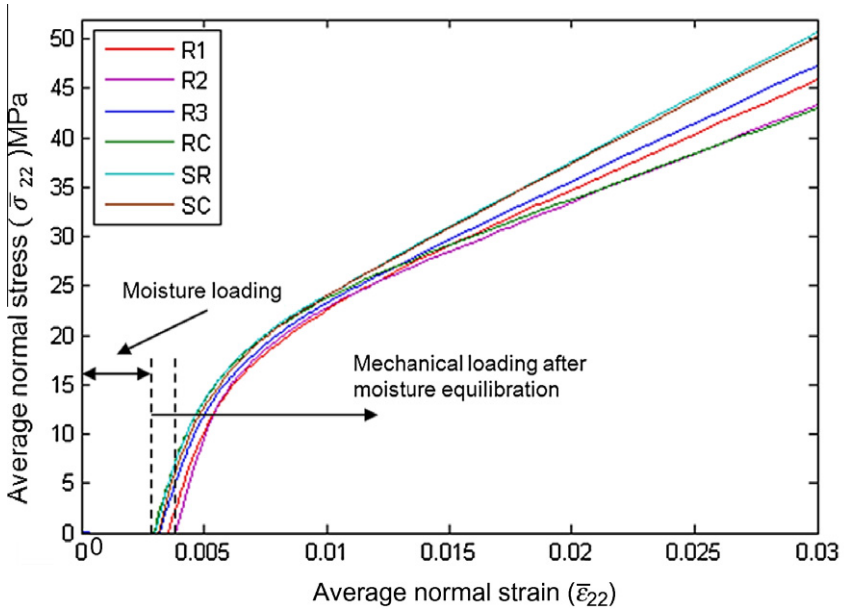

Fig. 8. Average normal stress ($\bar{\sigma}_{22}$)–normal strain ($\bar{\varepsilon}_{22}$) of the RVEs subjected to mechanical loading after moisture has equilibrated (moisture-affected interfaces). Moisture-resistant interfaces show a similar, but stronger response.

Table 2
Initial tangent moduli during the mechanical loading step of the sequential loading case.

RVE	Perfect interface (GPa)	Moisture-resistant interface		Moisture-affected interface	
		Modulus (GPa)	Variation from perfect interface (%)	Modulus (GPa)	Variation from perfect interface (%)
R1	11.5	9.6	17	8.8	23
R2	10.9	9.9	10	8.9	19
R3	11.7	8.8	25	7.8	33
RC	11.2	9.9	12	9.1	19
SR	13.6	10.9	20	9.8	28
SC	14.0	10.6	24	9.6	32

of columnar fiber arrangement the debonding is profuse at the fiber equatorial regions (90° to the poles) while the poles of the fibers remain connected to the matrix. Naturally, when loaded along the direction of the poles (X_2-direction) the RC arrangement is capable of carrying more stress by sharing it with the fibers than the SR, SC and R3, at least initially. The same argument holds true for the R1 and R2 arrangements too. At later stages though, debonding also evolves at the poles in the RC-RVE, but correspondingly the equators in the SR, SC and to some extent R3 do not, because at the equators the state of stress is predominantly compressive for the aligned fibers arrangements. Consequently, the RC topology (also, R1 and R2) suffers from a more severe overall softening elastic behavior compared to the SR, SC and R3 topologies (Fig. 8).

From these observations, we summarize that the overall stress–strain behaviors of the initially damaged microstructures exhibit similar qualitative trends irrespective of the RVE randomness. The lesser the initial damage in an RVE the better is its load carrying capacity. In addition, if the fiber arrangements are favorably aligned with the loading direction the damage accrues much more rapidly even if the initial (moisture-induced) damage is small (e.g. the SR-RVE). Taking this observation further, we posit that for the loading conditions simulating biaxial (tensile) stress states (as in the moisture diffusion scenario) it is the degree of clustering that decides the severity of damage; on the other hand, for uniaxial (or, significantly directionally biased) loading cases (e.g. the applied mechanical load scenario in this work) it is the alignment with reference to the primary loading direction that matters.

3.3. Effect of volume fraction and fiber diameter

We now generalize the damage characterization for RVEs with different f and diameter d. For consistent comparison, we restrict our attention to the damage sustained by different RVEs with moisture-affected interfaces at the end of the moisture loading step. As mentioned in Section 2.1, we calculate the coefficient of variation C_v for each RVE with three different r_c's.

As an illustration of the procedure used to correlate damage with C_v, Fig. 9a–c shows the correlation between ψ and C_v computed using different r_c's (Section 2.1), for a fixed $f = 0.50$ and $d = 10$ μm. The plots also indicate a linear fit along with the R^2 values. It can be seen that for these cases, the correlation is quite high. The same approach is adopted for a range of vf's ($f = 0.30$, 0.40 and 0.60) in addition to $f = 0.50$. For each f we considered an SR-RVE and five random arrangements. To incorporate the influence of d, we considered RVEs with $d = 9$ μm, 10 μm and 11 μm in these simulations.[6] For each RVE, ψ due to moisture diffusion was obtained from the FE simulations. Each ψ was then plotted separately against the C_v's of their corresponding RVEs based on the r_c's defined earlier and a linear regression was performed for each case (similar to Fig. 9a–c). Fig. 10 consolidates all these data where the R^2 values emerging from the linear regression analyses are plotted against f. It can be observed that high correlations between ψ and C_v are obtained for different r_c values across a range of f. While $r_c = 4.5r$ and

[6] Within a given RVE d is kept constant.

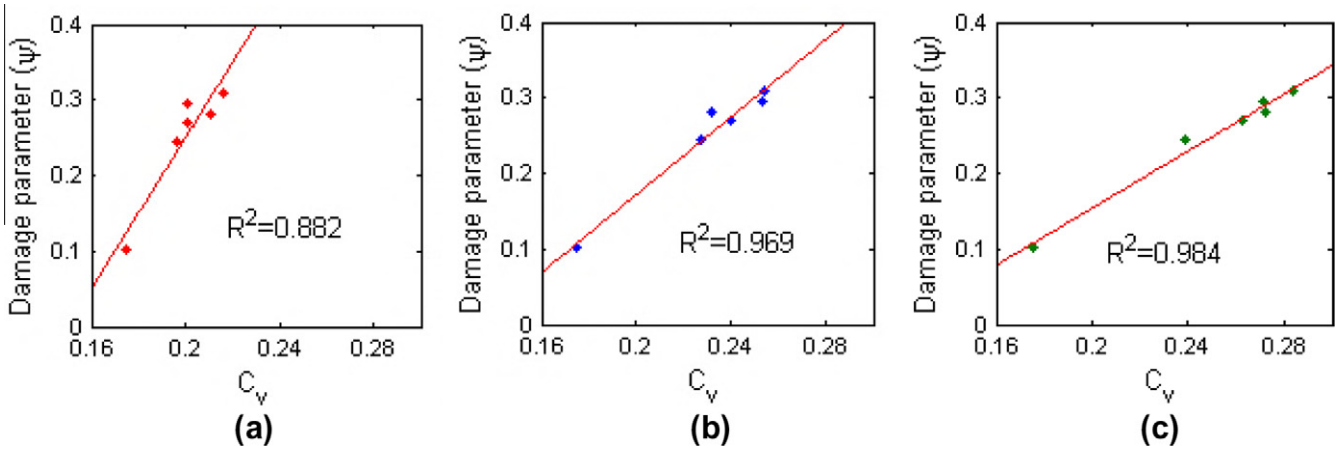

Fig. 9. ψ–C_v correlation for $f = 0.50$ with (a) $r_c = 4r$, (b) $r_c = 4.5r$, and (c) $r_c = 5r$. Moisture-affected interface cases.

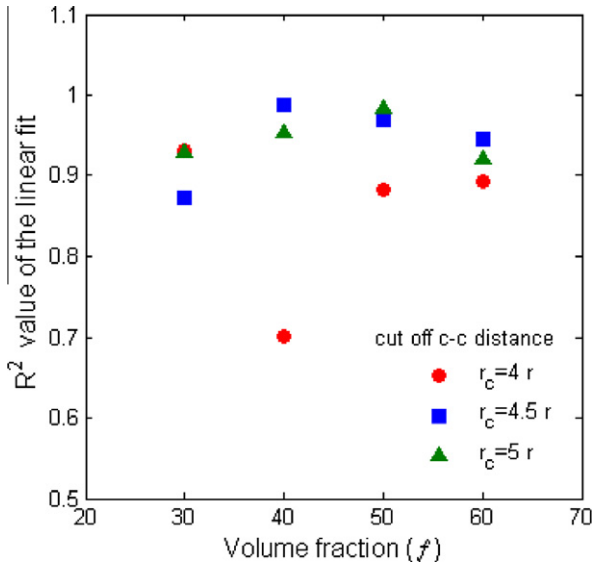

Fig. 10. Comparison of $C_v - \psi$ correlation for different fiber vf's determined from the linear regression (R^2) for different cut-off radii. Moisture-affected interfaces.

$r_c = 5r$ provided good correlations across all f's, the only reason for a relatively weaker correlation in the case of $r_c = 4r$ and $f = 0.40$ (Fig. 10) is due to one outlier in the random arrangement that had a C_v smaller than the SR-RVE (for $r_c = 4r$), but exhibited damage that was more severe than the SR-RVE for the same f.[7]

4. Summary and outlook

In this work we model the transient damage response of reinforced polymers subjected to the stresses induced due to moisture diffusion and mechanical loading. The study reveals that fiber distribution plays a significant role in the diffusion-induced residual stresses in a composite. This in turn determines the hot-spots for debonding, which may adversely affect the initial stiffness (e.g. in columnar fiber arrangement) or the overall stress (clustered arrangement). A trend that emerges from the results presented here is that the fiber clustering tends to hurt the performance of a composite over a period of time compared to the more regularly spaced arrangements [20]. The topological descriptor C_v characterizing the spatial inhomogeneity of fiber distribution is identified using the concept of cut-off radius that is motivated based on the mechanistic and geometric basis. The C_v correlates linearly with the overall diffusion-induced damage sustained for different RVEs over a range of fiber vf's and diameters; however, it does not enjoy a simple relationship with the tortuosity of an RVE owing to the highly directional nature of the later. An investigation of the synergistic effects of the moisture and mechanical loads indicates that moisture ingress assists the runaway microstructural failure that is dominated by the mechanical loading in the later stages. It is important to characterize the strength and toughness of interfaces in the presence of moisture as moisture-affected interfaces may not only cause significant degradation, but also accelerate the permeability through the channels that may form near the fibers. The degradation of the transverse stiffness of an RVE induced by initial moisture ingress also does not show a simple relation with C_v, again due to the directionality-induced complex interactions between the interfaces and the dominant loading direction. While this study uses the glass–fiber reinforced epoxy composite as a model system, some of the observations may be applicable in a variety of composites such as those used in dental restoration purposes or in pharmaceuticals. Our future work will focus on incorporating the mechanistic representation of the polymer degradation due to diffusion into its continuum constitutive description, viscoelastic relaxation mechanisms and investigating their impact on the composite microstructural response.

[7] Out of ~50 simulations that were performed for different cases, this was the only case that showed C_v lower than its SR counterpart. However, we chose to retain this in our results as it is important to know that there may be some peculiar cases, and we may need to explore a larger parametric space.

Acknowledgements

SPJ acknowledges financial support from NUS-AcRF-Tier 1 Grant # R-265-000-339-112. AM and LM, Jr acknowledge financial support by the Commission of the European Communities through the Sixth Framework Programme Grant UpWind, including UpWind.TTC (Contract #019945). The authors would like to thank the two anonymous reviewers for their constructive comments that led to significant improvement over the original version of the manuscript.

References

[1] Baley C, Davies P, Grohens Y, Dolto G. Application of interlaminar tests to marine composites. A literature review. Appl Compos Mater 2004;11:99.
[2] Hodzic A, Kim J, Lowe A, Stachurski Z. The effects of water aging on the interphase region and interlaminar fracture toughness in polymer–glass composites. Compos Sci Technol 2004;64:2185.

[3] Ferracane JL. Hygroscopic and hydrolytic effects in dental polymer networks. Dent Mater 2006;22:211.
[4] Derrien K, Gilormini P. The effect of applied stresses on the equilibrium moisture content in polymers. Scripta Mater 2007;56:297.
[5] Roy S, Vengadassalam K, Wang Y, Park S, Liechti KM. Characterization and modeling of strain assisted diffusion in an epoxy adhesive layer. Int J Solids Struct 2006;43:27.
[6] Weitsman Y. Coupled damage and moisture-transport in fiber-reinforced polymeric composites. Int J Solids Struct 1986;23:1003.
[7] Apicella A, Nicolais L, Astarita G, Drioli E. Effect of thermal history on water sorption, elastic properties and the glass transition of epoxy resins. Polymer 1979;20:1143.
[8] VanLandingham MR, Eduljee RF, Gillespie Jr JW. Moisture diffusion in epoxy systems. J Appl Polym Sci 1999;71:787.
[9] Xiao G, Shanahan M. Irreversible effects of hygrothermal aging on DGEBA/DDA epoxy resin. J Appl Polym Sci 1998;69:363.
[10] Xiao GZ, Delamar M, Shanahan MER. Irreversible interactions between water and DGEBA/DDA epoxy resin during hygrothermal aging. J Appl Polym Sci 1997;65:449.
[11] Xiao GZ, Shanahan MER. Water absorption and desorption in an epoxy resin with degradation. J Polym Sci B Polym Phys 1997;35:2659.
[12] Kensche CW. Fatigue of composites for wind turbines. Int J Fatigue 2006;28:1363.
[13] Choi HS, Ahn KJ, Nam JD, Chun HJ. Hygroscopic aspects of epoxy/carbon fiber composite laminates in aircraft environments. Composites Part A 2001;32:709.
[14] Wang SS, Chen X. Computational micromechanics for high-temperature constitutive equations of polymer–matrix composites with oxidation reaction, damage, and degradation. J Eng Mater Technol Trans ASME 2006;128:81.
[15] Chateauminois A, Vincent L, Chabert B, Soulier J. Study of the interfacial degradation of a glass–epoxy composite during hygrothermal ageing using water diffusion measurements and dynamic mechanical thermal analysis. Polymer 1994;35:4766.
[16] Weitsman Y, Guo YJ. A correlation between fluid-induced damage and anomalous fluid sorption in polymeric composites. Compos Sci Technol 2002;62:889.
[17] Tsenoglou CJ, Pavlidou S, Papaspyrides CD. Evaluation of interfacial relaxation due to water absorption in fiber–polymer composites. Compos Sci Technol 2006;66:2855.
[18] Gaur U, Chou C, Miller B. Effect of hydrothermal ageing on bond strength. Composites 1994;25:609.
[19] Ramirez F, Carlsson L, Acha B. Evaluation of water degradation of vinylester and epoxy matrix composites by single fiber and composite tests. J Mater Sci 2008;43:5230.
[20] Vaddadi P, Nakamura T, Singh RP. Transient hygrothermal stresses in fiber reinforced composites: a heterogeneous characterization approach. Composites Part A 2003;34:719.
[21] Vaddadi P, Nakamura T, Singh RP. Inverse analysis for transient moisture diffusion through fiber-reinforced composites. Acta Mater 2003;51:177.
[22] Roy S, Xu W, Patel S, Case S. Modeling of moisture diffusion in the presence of bi-axial damage in polymer matrix composite laminates. Int J Solids Struct 2001;38:7627.
[23] Loh W, Crocombe A, Abdel Wahab M, Ashcroft I. Modelling interfacial degradation using interfacial rupture elements. J Adhes 2003;79:1135.
[24] Lee S, Chiang H, Lin C, Huang H, Dong D. Finite element analysis of thermo-debonding mechanism in dental composites. Biomaterials 2000;21:1315.
[25] Bond D. Moisture diffusion in a fiber-reinforced composite. Part I – Non-Fickian transport and the effect of fiber spatial distribution. J Compos Mater 2005;39:2113.
[26] Kondo K, Taki T. Moisture diffusivity of unidirectional composites. J Compos Mater 1982;16:82.
[27] Mishnaevsky Jr L, Brøndsted P. Statistical modelling of compression and fatigue damage of unidirectional fiber reinforced composites. Compos Sci Technol 2009;69:477.
[28] Chen X, Papathanasiou T. Interface stress distributions in transversely loaded continuous fiber composites: parallel computation in multi-fiber RVEs using the boundary element method. Compos Sci Technol 2004;64:1101.
[29] Huang Y, Jin K, Ha S. Effects of fiber arrangement on mechanical behavior of unidirectional composites. J Compos Mater 2008;42:1851.
[30] Zhou XF, Wagner H, Nutt S. Interfacial properties of polymer composites measured by push-out and fragmentation tests. Composites Part A 2001;32:1543.
[31] Pyrz R, Bochenek B. Topological disorder of microstructure and its relation to the stress field. Int J Solids Struct 1998;35:2413.
[32] Torquato S. Nearest-neighbor statistics for packings of hard spheres and disks. Phys Rev E 1995;51:3170.
[33] Sevostianov I, Kushch V. Effect of pore distribution on the statistics of peak stress and overall properties of porous material. Int J Solids Struct 2009;46:4419.
[34] Kushch V, Shmegera S, Mishnaevsky Jr L. Statistics of microstructure, peak stress and interface damage in fiber reinforced composites. J Mech Mater Struct 2009;4:1089.
[35] ABAQUS/STANDARD 6.9; 2009. <http://www.simulia.com>.
[36] Yoon S, Jang C, Han B. Nonlinear stress modeling scheme to analyze semiconductor packages subjected to combined thermal and hygroscopic loading. J Electron Packag 2008;130:024502.
[37] González C, LLorca J. Mechanical behavior of unidirectional fiber-reinforced polymers under transverse compression: microscopic mechanisms and modeling. Compos Sci Technol 2007;67:2795.
[38] Wu C, Xu W. Atomistic simulation study of absorbed water influence on structure and properties of crosslinked epoxy resin. Polymer 2007;48:5440.
[39] De Neve B, Shanahan M. Physical and chemical effects in an epoxy resin exposed to water vapour. J Adhes 1995;49:165.
[40] De'Nève B, Shanahan MER. Water absorption by an epoxy resin and its effect on the mechanical properties and infra-red spectra. Polymer 1993;34:5099.
[41] Clancy T, Frankland S, Hinkley J, Gates T. Molecular modeling for calculation of mechanical properties of epoxies with moisture ingress. Polymer 2009;50:2736.
[42] Zhang H, Ericson M, Varna J, Berglund L. Transverse single-fibre test for interfacial debonding in composites: 1. Experimental observations. Composites Part A 1997;28:309.
[43] Shen L, Chen Z. Critical review of the impact of tortuosity on diffusion. Chem Eng Sci 2007;62:3748.